Improved contrast in laser-diode-based photoacoustic images with short-lag spatial coherence beamforming

Muyinatu A. Lediju Bell*, Xiaoyu Guo†, Hyun Jae Kang‡ and Emad Boctor‡§

*CISST Engineering Research Center, Johns Hopkins University, Baltimore, MD, USA
†Department of Electrical Engineering, Johns Hopkins University, Baltimore, MD, USA
‡Department of Computer Science, Johns Hopkins University, Baltimore, MD, USA
§Department of Radiology, Johns Hopkins University, Baltimore, MD, USA

Abstract—Pulsed laser diodes (PLDs) enable photoacoustic imaging with lower cost, increased portability, and higher frame rates compared to conventional Q-switched Nd:YAG lasers. However, the main disadvantage of the PLD is its low peak power, which necessitates averaging thousands of photoacoustic signals to achieve signal-to-noise ratios that are comparable to those produced by an Nd:YAG laser. The averaging process degrades temporal resolution with minimal improvements to image contrast. This work is the first to investigate the use of a PLD and short-lag spatial coherence (SLSC) beamforming to display high-contrast photoacoustic images with minimal to no signal averaging required. The mean contrast in single photoacoustic images of targets as deep as 5-15 mm from the surface was improved by 11-17 dB with SLSC beamforming when compared to conventional delay-and-sum (DAS) beamforming of the same data. The SLSC correlation kernel was adjusted based on laser pulse lengths to demonstrate applicability to coded excitation. Results suggest that coherence-based beamforming can overcome current limitations with real-time PLD-based photoacoustic imaging.

I. INTRODUCTION

Photoacoustic (PA) imaging is implemented by transmitting pulsed laser light to a target. The target absorbs the light, undergoes thermoelastic expansion, and generates sound waves that are detectable with a conventional ultrasound probe. Typical laser sources for PA imaging (e.g. Q-switched Nd:YAG lasers) are bulky and thus not easily portable. In addition, these lasers are expensive, with low pulse repetition frequencies (e.g. tens of Hertz), and not sufficiently suitable for real-time 2D and 3D imaging. They additionally output energies on the order of millijoules (mJ), which raises safety concerns.

A pulsed laser diode (PLD) is a smaller, less expensive alternative [1] with kHz pulse repetition frequencies (PRFs) and energy outputs on the order of microjoules (μJ). Potential clinical applications include visualization of superficial *in vivo* blood vessels [2], blood cancer testing [3], and 3D imaging [4]. However, photoacoustic signal amplitudes proportionally scale with the laser energy, and thus the lower energy output of the PLD produces photoacoustic channel data with low SNR, which necessitates averaging thousands of PA signals to achieve similar channel SNR to that produced by a Q-switched laser [2], [5]. This averaging step reduces frame rates with minimal improvements to target contrast.

We previously demonstrated in phantoms, *ex vivo* tissue, and *in vivo* that the short-lag spatial coherence (SLSC) beamformer is not susceptible to low laser energies when compared to more conventional amplitude-based beamformers such as delay-and-sum (DAS) or fast Fourier transform-based reconstruction methods [6]–[8], hence it offers better contrast

even at low laser energies. Pourebrahimi *et al.* [9] additionally demonstrated that the SLSC beamformer outperforms DAS by reducing clutter and improving resolution when imaging spherical and point targets, respectively. These improvements were achieved because the SLSC beamformer, which was initially developed for ultrasound imaging [10]–[12], considers the spatial coherence of a received wavefield rather than signal amplitude. Thus, we propose short-lag spatial coherence beamforming to overcome the most outstanding limitation of PLDs for photoacoustic imaging – i.e. poor target contrast in single images – caused by the low peak output power.

II. METHODS

A. Experimental Setup

A block diagram of the experimental system setup to test the SLSC beamformer with PLD-based PA data is shown in Fig. 1. A plastisol phantom was attached to the face of a 128-element Ultrasonix L14-5W/60 linear array probe with a bandwidth of 5-14 MHz. The phantom contained three 4-mm diameter cylindrical black rubber targets embedded at depths of 5, 11, and 15 mm from the exposed surface. In addition, this phantom was replaced with a 7 mm thick slab of liver tissue and a 7 mm thick two-layer tissue-plastisol phantom to investigate the system for interventional applications that require photoacoustic visualization of the tissue surface [13]. In the two-layer phantom, liver tissue was attached to the face of the probe and the plastisol (dyed black) was exposed.

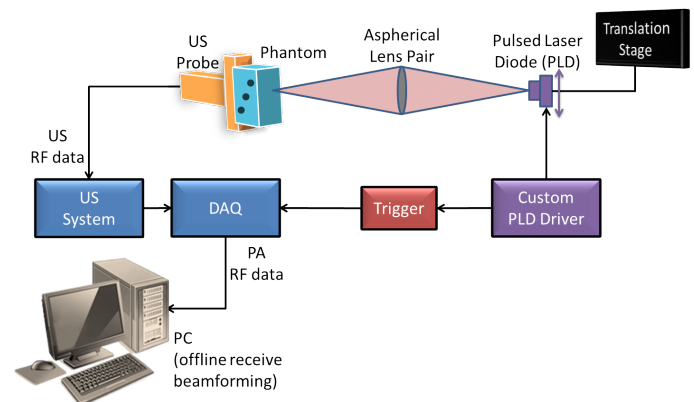A single diode laser was driven with a 50-100 ns pulse at a

Fig. 1. Block diagram of experimental setup. Ultrasound (US) data were collected with the SonixTouch when the laser was off. Photoacoustic (PA) data were acquired with the SonixDAQ, triggered by a custom PLD driver, and sent to a personal computer (PC) for data storage and off-line processing.

rate of 500 pulses per second by a custom driver. In a separate experiment, the PLD was driven with a 900 ns pulse train (five consecutive pulses of duration 100 ns, each separated by 100 ns) at a rate of 500 pulse trains per second to investigate beamformer performance for coded excitation applications. The pulse energy ranged 2.4-8 μJ. The resulting 905 nm wavelength laser beam was air-coupled to an aspherical lens pair, directed in line with the transducer, and focused on the phantom.

The PLD was attached to a manual translation stage to control the focus of the laser beam in the lateral dimension of the transducer in 0.635 mm increments. The probe was connected to an Ultrasonix SonixTouch ultrasound system to acquire ultrasound data when the laser was off. An Ultrasonix data acquisition unit (SonixDAQ, BC, Canada) was connected to one of the transducer ports on the ultrasound system and triggered by the custom PLD driver to acquire raw pre-beamformed PA channel data at sampling and frame rates of 40 MHz and 5 Hz, respectively.

B. Beamforming of PLD Photoacoustic Signals

To increase the SNR of photoacoustic signals acquired with a PLD, each RF line may be averaged over multiple frames prior to implementing DAS or SLSC beamforming, as described by the following equation:

$$s'_i(n) = \frac{1}{T} \left[\sum_{t=1}^{T} s_i(n, t) \right] \tag{1}$$

where s_i represents the time-delayed, zero-mean signal received by the ith transducer element, n is the axial sample depth in units of samples, t is the RF frame number, and T is the total number of frames that are averaged.

To form SLSC images, a coherence curve was calculated by computing the normalized cross-correlation between the time averaged channel data (s'_i) received by an array with N total elements over an axial kernel length of $k = n_2 - n_1$ [10]:

$$\hat{R}(m) = \frac{1}{N-m} \sum_{i=1}^{N-m} \frac{\sum_{n=n_1}^{n_2} s'_i(n) s'_{i+m}(n)}{\sqrt{\sum_{n=n_1}^{n_2} s'^2_i(n) \sum_{n=n_1}^{n_2} s'^2_{i+m}(n)}} \tag{2}$$

where m is the distance (i.e. lag) between two elements of the receive aperture in units of number of elements. Note that the correlations are averaged to produce a single coherence estimate for each lag. Unless otherwise stated, k was equivalent to the smallest wavelength within the bandwidth of the linear array (i.e. 9 samples). One SLSC image pixel is the integral of coherence curves up to a preselected short-lag value, M:

$$SLSC(x, z) = \sum_{m=1}^{M} \hat{R}(m), \tag{3}$$

where x and z correspond to the lateral and axial spatial dimensions of the pixel, respectively, both in units of mm. The short lag value may be adjusted to optimize image performance, as demonstrated previously [6], but throughout this paper, it was held constant at $M = 4$ to investigate the changes that occur as T is varied. These changes were quantified using the target contrast and SNR (calculated from beamformed RF data), channel SNR, and coherence curves.

III. RESULTS AND DISCUSSION

A. Vessel Phantom

Photoacoustic data were acquired with the laser focused on the the center vessel target. The pulse energy was 2.4 μJ. The target was present in single (T=1) and averaged (T=100) DAS images, as shown in Fig. 2(a) and (c), respectively, however, this target is difficult to visualize due to electronic noise and poor channel SNR. The target is better visualized in the corresponding SLSC images in Fig. 2(b) and (d) created from the same channel data (T=1 and 100, respectively).

The contrast and SNR of the target in Fig. 2 was quantified as T was varied from 1-159, as shown in Fig. 3(a) and (b),
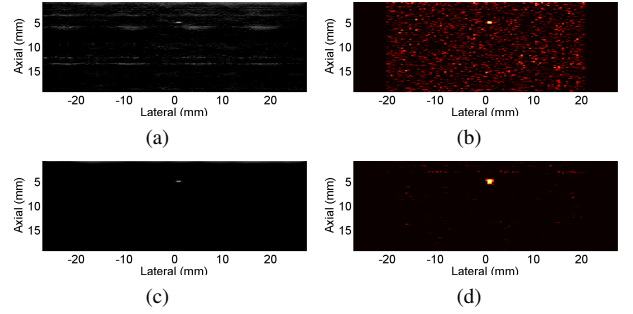

Fig. 2. (a,c) DAS and (b,d) SLSC images of (a,b) one frame (i.e. T=1) and (c,d) 100 frames averaged prior to beamforming. All images are shown with 20 dB dynamic range.
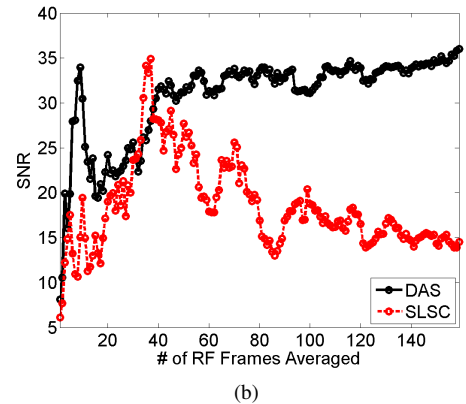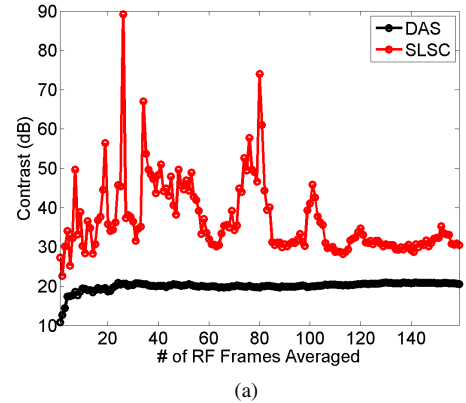

Fig. 3. Target contrast and SNR in SLSC and DAS images as a function of the number of frames averaged.

respectively. Contrast is 8-69 dB higher with SLSC imaging compared to DAS images. In addition, the contrast increase of the DAS image appears to reach a plateau after averaging approximately 30 RF frames, while the contrast of the SLSC images experiences more variation from frame to frame. Although contrast is improved with SLSC beamforming, the SNR of the vessel target is similar or up to a factor of 3 better with DAS beamforming.

Coherence curves for the maximum signal in SLSC images of the center vessel target are shown in Fig. 4 for four values of T. In all cases, the coherence of the peak signal is higher than that of the noise, and this difference is the main source of contrast in SLSC images. Note that coherence generally increases as the number of averaged frames (i.e. T) increases.

Fig. 5(a) shows the mean coherence at $M = 4$ as the number of averaged frames increases. In addition, the coherence length, measured at a coherence of 0.3 (Fig. 5(b)), rapidly increases over a small number of averaged RF frames while the channel SNR has a more gradual increase. The observed changes in coherence, coherence length, and channel SNR and the corresponding improved contrast in SLSC and DAS images within the first few values of T (Fig. 3) indicate that DAS and SLSC contrast are both better when signals are more coherent and clutter is reduced. On the other hand, the SNR of the DAS image steadily increases with T likely because the channel SNR steadily increases, with the exception of a sharp increase early in time that could be caused by the sharp increase in coherence length between 1 and 5 frames.

The ultrasound image of the vessel phantom with the vessels encircled and numbered is shown in Fig. 6 (top), along with the corresponding DAS and SLSC photoacoustic images created from the same channel data ($T = 15$) as the laser was translated in the probe's lateral dimension (Fig. 6, middle and bottom, respectively). The target farthest from the light source and closest to the probe (i.e. Vessel 1) is the most difficult to visualize with the DAS beamformer, because of the lower laser fluence incident on this target. The three targets are better visualized with SLSC beamforming, as summarized with the contrast values in Table I. *In vivo* blood vessels were previously visualized 1 mm below the surface [2], and the results herein
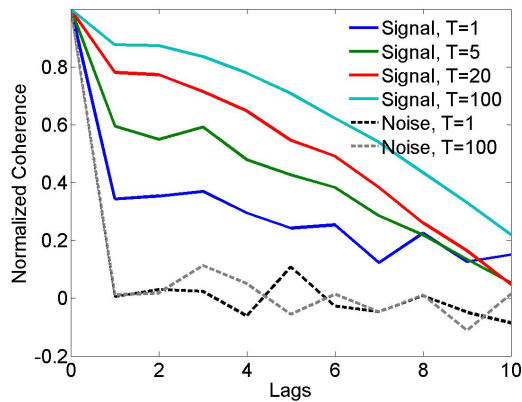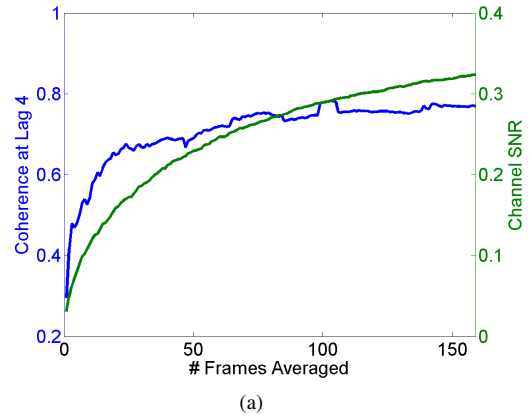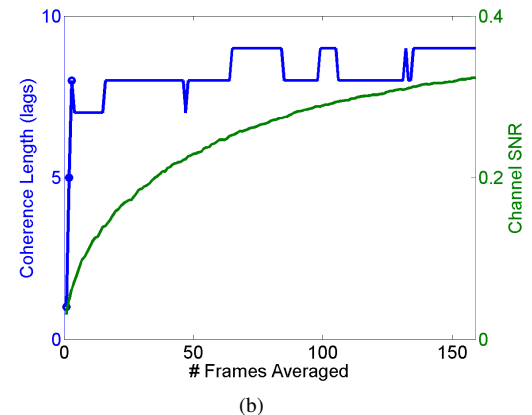

(a)

(b)

Fig. 5. Channel SNR displayed with (a) the coherence at lag 4 and (b) the coherence length (at 0.3) as function of the number of frames averaged.

indicate that targets as deep as 5-15 mm from the surface may be visualized with the SLSC beamformer.

B. Surface Targets

In addition to the phantom with embedded vessel-like targets, the laser was focused on the surface of black plastisol and liver tissue. This setup is relevant to interventional photoacoustic applications that employ direct registration of photoacoustic and stereo camera images [13]. Similar to the vessel phantom, these targets were visualized with 7-13 dB better contrast in SLSC images compared to DAS images, as reported in Table I.

Fig. 4. Coherence of peak signal in SLSC PA images when the number of averaged frames (T) = 1, 5, 20, and 100, compared to that of noise when T= 1 and 100.

TABLE I. MEAN CONTRAST OF ≥ 10 SINGLE FRAME (T=1) DAS AND SLSC IMAGES OF EMBEDDED AND SURFACE PHOTOACOUSTIC TARGETS

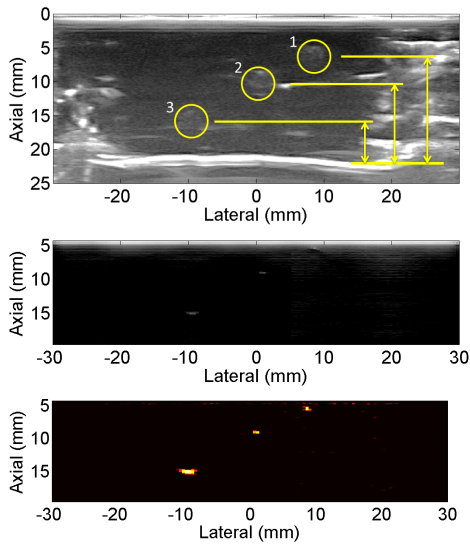| Target	Pulse Duration (ns)	Pulse Energy (μJ)	Distance from Surface (mm)	DAS Contrast (dB)	SLSC Contrast (dB)
Embedded					
Vessel 1	50	2.4	15	3	14
Vessel 2	50	2.4	11	13	27
Vessel 3	50	2.4	5	10	27
Surface					
Ex vivo liver tissue	100	8	-	11	24
Plastisol + tissue	100	7	-	22	29
Plastisol + tissue	900	7	-	22	30
Plastisol + tissue	100	7	-	22	30*
Plastisol + tissue	900	7	-	22	32*

*Axial kernel length, k, was 41 samples.

Fig. 6. Ultrasound B-mode image of vessel phantom (top) and combined DAS (middle) and SLSC (bottom) images as the laser was translated to visualize the three vessel targets ($T = 15$). Arrows indicate vessel distance from exposed surface. The DAS and SLSC images are shown with 30 dB and 20 dB dynamic range, respectively.

C. Coded Excitation

After transmitting a 900 ns pulse train (Fig. 7(a)), SLSC images were created with a correlation kernel similar to the pulse train length (i.e. $k = 41$), as shown in Fig. 7(c). When a single laser pulse was transmitted (Fig. 7(b)), with the same SLSC parameters, the axial FWHM of the signal was 1.2 mm shorter (Fig. 7(d)). When these same data were beamformed with $k = 9$, the axial FWHM differed by less than 0.1 mm, as shown in Fig. 7(e) and (f). In corresponding DAS images (Fig. 7(g) and (h), respectively), the FWHM difference is 0.4 mm. These results indicate that the measured FWHM differences are caused by the unique pulse signatures, detection of the
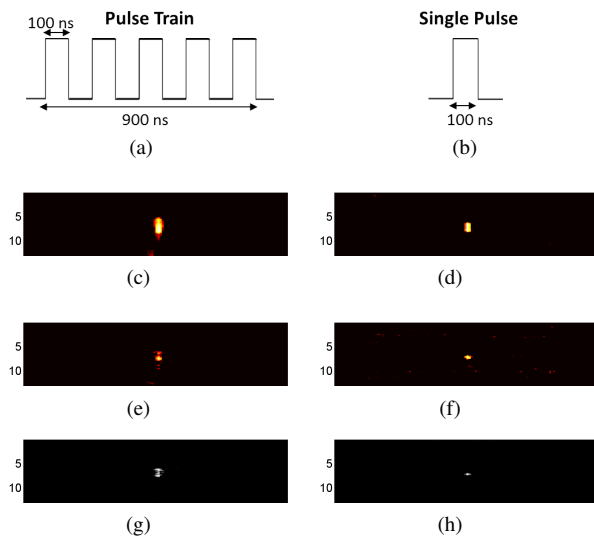

Fig. 7. SLSC photoacoustic images (T=1) were created with the laser pulses illustrated in (a) and (b) and correlation kernel length, k, equal to 41 samples (c,d, respectively) and 9 samples (e,f, respectively). (g,h) Corresponding DAS photoacoustic images formed with the laser pulses shown in (a) and (b), respectively. All images shown with 20 dB dynamic range and a mm scale.

coherent pulse train signature depends on the value of k, which can be adjusted to detect unique coded excitation signatures with greater sensitivity (i.e. greater FWHM differences) than conventional DAS beamforming.

IV. CONCLUSION

SLSC beamforming overcomes the most outstanding limitation of PLDs for photoacoustic imaging. Fewer RF frames were averaged with better contrast than conventional DAS beamforming of the same number of frames, and a small number of correlation lags (i.e. $M = 4$) were utilized. In addition, targets as deep as 15 mm were better visualized with the SLSC beamformer, and unique pulse signatures were detected by adjusting the correlation kernel length, k, to match the pulse length. These improvements make PLDs an even more attractive option for real-time clinical applications, including vessel imaging, direct photoacoustic to stereo camera registration, and coded excitation.

REFERENCES

[1] T J Allen and P C Beard. Dual wavelength laser diode excitation source for 2D photoacoustic imaging. In *Biomedical Optics (BiOS) 2007*, pages 64371U–64371U. International Society for Optics and Photonics, 2007.

[2] R GM Kolkman, W Steenbergen, and T G van Leeuwen. In vivo photoacoustic imaging of blood vessels with a pulsed laser diode. *Lasers in Medical Science*, 21(3):134–139, 2006.

[3] E I Galanzha, E V Shashkov, P M Spring, J Y Suen, and V P Zharov. In vivo, noninvasive, label-free detection and eradication of circulating metastatic melanoma cells using two-color photoacoustic flow cytometry with a diode laser. *Cancer Research*, 69(20):7926–7934, 2009.

[4] L Zeng, G Liu, D Yang, and X Ji. 3D-visual laser-diode-based photoacoustic imaging. *Optics Express*, 20(2):1237–1246, 2012.

[5] T J Allen and P C Beard. Pulsed near-infrared laser diode excitation system for biomedical photoacoustic imaging. *Optics Letters*, 31(23):3462–3464, 2006.

[6] M A Lediju Bell, N Kuo, D Y Song, and E M Boctor. Short-lag spatial coherence beamforming of photoacoustic images for enhanced visualization of prostate brachytherapy seeds. *Biomedical Optics Express*, 4(10):1964, 2013.

[7] M A Lediju Bell, D. Y. Song, and E. M. Boctor. Coherence-based photoacoustic imaging of brachytherapy seeds implanted in a canine prostate. In *SPIE Medical Imaging*, 2014.

[8] M A Lediju Bell, N P Kuo, Danny Y Song, J Kang, and E M Boctor. In vivo photoacoustic imaging of prostate brachytherapy seeds. In *SPIE BiOS*, pages 894348–894348, 2014.

[9] B Pourebrahimi, S Yoon, D Dopsa, and M C Kolios. Improving the quality of photoacoustic images using the short-lag spatial coherence imaging technique. In *SPIE BiOS*, pages 85813Y–85813Y, 2013.

[10] M. A. Lediju, G. E. Trahey, B. E. Byram, and J. J. Dahl. Short-lag spatial coherence of backscattered echoes: Imaging characteristics. *IEEE Transactions on Ultrasonics, Ferroelectrics and Frequency Control*, 58(7):1337, 2011.

[11] M A Lediju Bell, R Goswami, J A Kisslo, J J Dahl, and G E Trahey. Short-lag spatial coherence imaging of cardiac ultrasound data: Initial clinical results. *Ultrasound in Medicine & Biology*, 39(10):1861–1874, 2013.

[12] J. J. Dahl, D. Hyun, M. A. Lediju, and G. E. Trahey. Lesion detectability in diagnostic ultrasound with short-lag spatial coherence imaging. *Ultrasonic Imaging*, 33(2):119, 2011.

[13] A Cheng, J U Kang, R H Taylor, and E M Boctor. Direct three-dimensional ultrasound-to-video registration using photoacoustic markers. *Journal of Biomedical Optics*, 18(6):066013–066013, 2013.